Primary Multiparametric Quantitative Brain MRI: State-of-the-Art Relaxometric and Proton Density Mapping Techniques

Hernán Jara, PhD; Osamu Sakai, MD, PhD; Ezequiel Farrher, PhD; Ana-Maria Oros-Peusquens, PhD; N. Jon Shah, PhD; David C. Alsop, PhD; Kathryn E. Keenan, PhD

Abstract

This review on brain multiparametric quantitative MRI (MP-qMRI) focuses on the primary subset of quantitative MRI (qMRI) parameters that represent the mobile ("free") and bound ("motion-restricted") proton pools. Such primary parameters are the proton densities, relaxation times, and magnetization transfer parameters. Diffusion qMRI is also included because of its wide implementation in complete clinical MP-qMRI application. MP-qMRI advances were reviewed over the past 2 decades, with substantial progress observed toward accelerating image acquisition and increasing mapping accuracy. Areas that need further investigation and refinement are identified as follows: (a) the biologic underpinnings of qMRI parameter values and their changes with age and/or disease and (b) the theoretical limitations implicitly built into most qMRI mapping algorithms that do not distinguish between the different spatial scales of voxels versus spin packets, the central physical object of the Bloch theory. With rapidly improving image processing techniques and continuous advances in computer hardware, MP-qMRI has the potential for implementation in a wide range of clinical applications. Currently, three emerging MP-qMRI applications are synthetic MRI, macrostructural qMRI, and microstructural tissue modeling.

From the Department of Radiology, Boston University, 670 Albany St, Boston, Mass 02118 (H.J., O.S.); Institute of Neuroscience and Medicine-4, Forschungszentrum Jülich, Jülich, Germany (E.F., A.M.O.P., N.J.S.); Department of Radiology, Beth Israel Deaconess Medical Center, Harvard Medical School, Boston, Mass (D.C.A.); and Physical Measurement Laboratory, National Institute of Standards and Technology, Boulder, Colo (K.E.K.).
Received June 16, 2021; revision requested August 20; revision received May 1, 2022; accepted May 24.
Address correspondence to H.J. (email: hjara@bu.edu).

Contemporary clinical MRI consists of a mosaic of differently weighted images, which carry qualitative information based on nonstandardized pixel value scales. Quantitative MRI (qMRI) seeks to quantify a limited number of tissue parameters at the pixel scale and display quantitative images known as maps. Though early attempts at qMRI were slow and often resulted in poor map quality, a confluence of factors has reignited interest. One factor is the increased pressure for pixel value standardization. Expanding health care and computer networks have streamlined digital access to images acquired across sites and scanners, but differences in scanners and protocols make medical comparisons difficult. This hinders optimum patient care and limits the biologic insight of MRI data. Another factor for renewed interest in qMRI is the development of fast multiparametric acquisition methods, where accelerated or undersampled images are combined with physical models to reconstruct images of multiple qMRI tissue parameters rapidly. qMRI maps can be assessed visually or processed to simulate any desired image acquisition protocol, a process known as synthetic MRI. Multiparametric qMRI (MP-qMRI) also facilitates the use of thresholds or region of interest averages as diagnostic criteria that can be assessed in multisite studies. Perhaps more importantly, there is increasing evidence that MP-qMRI of proton density (PD), T_1, and T_2 could provide the normal distributions of these parameters, which may help assess neurologic diseases (1) as deviations from healthy brain development across the human lifespan (2–5). Such quantitative assessment could be sensitive for detecting early disease.

The purpose of this review within the MRI physics context is to provide a structured survey of MP-qMRI of the brain, with a focus on technical developments for a subset of parameters of the mobile (“free”) and macromolecular (“motion-restricted”) proton pools, specifically the PDs, relaxation times, and magnetization transfer (MT) parameters. We will discuss diffusion MRI (dMRI) because of its high clinical importance and because the basic MP-qMRI field incorporates diffusion parameters (6–8). For deeper insights into the physics and applications of dMRI, the reader is directed to a review by Le Bihan and Johansen-Berg (9). The present review on MP-qMRI fits within the goals of the initiative of the Quantitative Imaging Biomarkers Alliance (10), which seeks to improve the value and practicality of quantitative imaging biomarkers by reducing variability across devices, sites, patients, and time.

Abbreviations

ADC = apparent diffusion coefficient, BPP = Bloembergen, Purcell, and Pound, CSF = cerebrospinal fluid, dMRI = diffusion MRI, GM = gray matter, MP-qMRI = multiparametric qMRI, MRF = MR fingerprinting, MT = magnetization transfer, MTM = microstructural tissue modeling, PD = proton density, qMRI = quantitative MRI, WM = white matter

Summary

Multiparametric quantitative MRI of the brain has the potential for implementation in a wide range of clinical applications.

Essentials

- Modern multiparametric quantitative MRI (MP-qMRI) frameworks consist of fast multicontrast pulse sequences and mapping algorithms that model the pulse sequence with use of MRI theory.
- Whole-brain MP-qMRI frameworks encompassing proton density, MR relaxation times, and the diffusion property may function as a complete neuroimaging protocol in less than 10 minutes of acquisition time.
- Three promising MP-qMRI applications are synthetic MRI, macrostructural quantitative MRI, and microstructural tissue modeling.

Physics Context

qMRI Frameworks

qMRI parameters can be mapped individually or in groups with MP-qMRI frameworks that consist of an MP-qMRI pulse sequence and a theory-matched qMRI mapping algorithm. Theoretical matching consists of modeling the pulse sequence with use of the Bloch theory (11), with possible extensions to include the effects of MT (12) and/or diffusion (13). Early MP-qMRI frameworks were described soon after the advent of clinical MRI (14–17) before the advent of scanning acceleration techniques. Therefore, the quantification and imaging acquisition were time consuming and clinically impractical compared with weighted (qualitative) MRI pulse sequences, such as T_1- and T_2-weighted imaging. Additionally, early qMRI maps were often less appealing visually relative to qualitative weighted images (15,16,18). Contemporary MP-qMRI frameworks bear improvements in speed, quantitative accuracy, and multiparametricity. Several frameworks could be used as a complete neuroimaging protocol with a total scan time of about 10 minutes (7,19,20).

Numerous fast MP-qMRI frameworks have been described in the past 3 decades (Tables 1, 2). We identify two distinct and heterogeneous framework types based on pulse sequence design and the type of imaging data acquired. First, fast indirect frameworks with fully reconstructed weighted images are used as an intermediate step for map generation. Second, fast direct qMRI frameworks using imaging data fragments–“fingerprints” and “tasks”–are used directly for map generation. This is the case in MR fingerprinting (MRF) (21–24) and MR multitasking (7), respectively.

Because the magnetization dynamics during the pulse sequence execution obey the laws of MR theory, the purpose of the qMRI algorithm is to model the pulse sequence according to these laws and use the model for inferring the qMRI parameter values that best describe the experimental data on a voxel-by-voxel basis. Accordingly, qMRI parameter estimates are generated by associating theoretical predictions of the mapping algorithm with experimental data generated by the MP-qMRI pulse sequence. Increasing the number of qMRI parameters of a multiparametric MRI method can necessitate a longer scan time; however, the added scan time is typically less than serially acquiring individual parametric qMRI measurements. Furthermore, the benefits of increasing multiparametricity are considerable if the objective is to build a comprehensive quantitative representation of the patient. Such multidimensional quantitative representation modeling of the patient could serve as a virtual analog of each patient for a variety of postprocessing applications that broaden the scope of qMRI. Important image processing applications include (a) synthetic MRI for enhanced and comprehensive visual exploration of contrast weightings, (b) macrostructural qMRI for data reduction and the generation of data reports that include volumetrics and tissue quality measures, and (c) microstructural tissue modeling (MTM) for deciphering the intravoxel milieu.

Table 1: Fast Indirect Multiparametric qMRI Frameworks

Readout	Pulse Sequence	Parameters	Year(s)	Reference(s)
EPI	ms-DSEPI-T12: multishot double spin-echo EPI	T1, T2	2010	76
EPI	STEM: stimulated echo mapping	T1, T2, ADC	2019	69
EPI	ZEBRA: Z-location shuffling, multiple echoes, and B-interleaving for relaxometry-diffusion acquisitions	T1, T2*, ADC	2018	77
EPI	Multi-inversion multiecho spin- and gradient-echo EPI	T1, T2, T2*, PD	2021	78
RARE	TCRARE: triple-contrast RARE sequence	T1, T2, PD	1993	79
RARE	Mixed TSE: mixed turbo spin echo	T1, T2, PD	2006, 2009	3, 4
RARE	Triple turbo spin echo	T1, T2, PD	2017	80
RARE	Standard turbo spin-echo images	T1, T2	2019	19
RARE	QRAPMASTER: quantification of relaxation times and proton density by multiecho acquisition of a saturation recovery using turbo spin-echo readout	T1, T2, PD	2008	81
GE	STAGE: strategically acquired GE	T1, T2*, PD	2020	82
SS	Multiple-echo GE	T2*, PD	2019	83
SS	DESPOT1 and DESPOT2: driven equilibrium single-pulse observation of T1 and T2	T1, T2	2003, 2005	84, 85
SS	IR-TrueFISP: inversion-recovery true fast imaging with SS precession	T1, T2, PD	2004	86
SS	IR-bSSFP: inversion-recovery balanced SSFP	T1, T2, PD	2010	87
SS	IR-TrueFISP: inversion-recovery true fast imaging with SS precession (golden ratio–based radial readout)	T1, T2, PD	2012	88
SS	MP-DESS: magnetization-prepared double-echo SS	T1, T2, PD	2014	89
SS	TESS: triple-echo SS relaxometry	T1, T2, PD	2014	90
SS	Multiple 3D bSSFP: Multiple 3D balanced SSFP	T1, T2, T2*, PD	2015	91
SS	MIRACLE: motion-insensitive rapid configuration relaxometry	T1, T2	2017	92
SS	DW-DESS: diffusion-weighted dual-echo SS	T1, T2, ADC, PD	2017	93
SS	SMS-TESS: simultaneous multislice triple-echo SS	T1, T2, PD	2018	94
SS	PLANET: ellipse-fitting approach for simultaneous T1 and T2 mapping using phase-cycled balanced SSFP	T1, T2	2018, 2019	95, 96
SS	MPME: multipathway multiecho imaging	T1, T2, PD	2019	97
SS	Alternating unbalanced SSFP for 3D mapping of the human brain	T2*, T2	2021	98
LL	3D-QALAS: 3D quantification using an interleaved LL acquisition sequence with T2 preparation pulse	T1, T2, PD	2020	99

Note.—These frameworks generate full frame-weighted images and use these as input to the quantitative MRI (qMRI) mapping algorithms. Frameworks are organized by type of acceleration technique and then listed in chronological order. 3D = three-dimensional, ADC = apparent diffusion coefficient, EPI = echoplanar imaging, GE = gradient echo, LL = Look-Locker, PD = proton density, RARE = rapid acquisition with relaxation enhancement, SS = steady state, SSFP = SS free precession.

Table 2: Fast Direct Multiparametric Quantitative MRI Frameworks

Readout	Pulse Sequence	Parameters	Year(s)	Reference(s)
SS	bSSFP with MRF framework	T1, T2, PD	2013	21
SS	SS free precession with MRF framework	T1, T2, PD	2015	22
SS	3D MR fingerprinting using parallel imaging and deep learning	T1, T2, PD	2020	20
SS	3D multiparametric MRI with quantitative transient-state imaging	T1, T2	2020	24
Segmented FLASH	3D MR multitasking	T1, T2, ADC	2020	7, 8
SS	Hybrid-state free precession in nuclear MR	T1, T2	2019	100

Note.—These frameworks are used to acquire imaging data fragments (MR fingerprints [101] or task) and proceed to map calculation, bypassing the weighted image generation step. Frameworks are organized by type of acceleration technique. 3D = three-dimensional, ADC = apparent diffusion coefficient, bSSFP = balanced SS free precession, FLASH = fast low-angle shot, PD = proton density, SS = steady state.

Spatial Scales

MRI physics deals with a wide range of spatial scales that span about 12 orders of magnitude, starting from ^{1}H nuclei at a spatial scale of 10^{-6} nm to that of the water molecule at a spatial scale of 10^{-1} nm to the spatial scale of spin packets at about 10 nm (see next paragraph) and up to the spatial scale of current clinical imaging voxels of less than 10^{6} nm (,1 mm). qMRI algorithms use primarily semiclassical MR theory (ie, the Bloch equation, with possible extensions to include the effect of diffusion with the Bloch-Torrey equation [13] or MT and chemical exchange with the Bloch-McConnell equations [12]).

Spin packets are subvoxel moieties similar to spin isochromats, but instead of being defined by a unique precession frequency, spin packets are associated with a unique diffusion coefficient (25) and therefore are characterized by a unique molecular correlation time (τ_c), given that τ_c 1/D, where D is the diffusion coefficient. The correlation time is a unifying concept that links the three spatial scales of relevance to qMRI theory (Fig 1). The spatial scale of spin

packets is imprecisely defined; on one hand, Bloch theory requires spin packets to be much larger than the water molecule so that number of contained spins is sufficiently large and the laws of statistical mechanics apply. On the other hand, the theory also calls for microscopic spin packets so that the intravoxel magnetization distribution can be modeled as a continuous function of space and time. In a hypothetical model, we can imagine spin packets as small cubes containing about 10 000 water molecules to guarantee the appropriateness of the statistical mechanics description. Considering that the diameter of a water molecule is approximately 0.34 nm, the linear dimension of such a spin packet is estimated to be about 10 nm, which is about one-third the spacing between myelin sheaths (26).
Importantly, the mismatch in voxel scale to spin-packet scale results in major inconsistencies in most qMRI algorithms, which compare theoretical information pertaining to the spin-packet scale against voxel scale experimental information. This theoretical inconsistency needs to be addressed in future qMRI algorithm developments by using a realistic description of the actual voxel shapes of Fourier transform imaging (Fig 1) by means of the voxel sensitivity function (27). In addition, such theoretical efforts could be useful for probing the intravoxel milieu with relaxometry-based mapping of tissue microstructure (28,29), which has been traditionally investigated using dMRI (30–34).

Relaxation Theory

The quantum theory that first explained the main MR relaxation mechanisms was proposed by Bloembergen, Purcell, and Pound (BPP) (35). It revealed that MR relaxation is caused by protondipole interactions with the time-varying magnetic field of the neighbor protons. The BPP theory accurately models simple aqueous systems, such as healthy

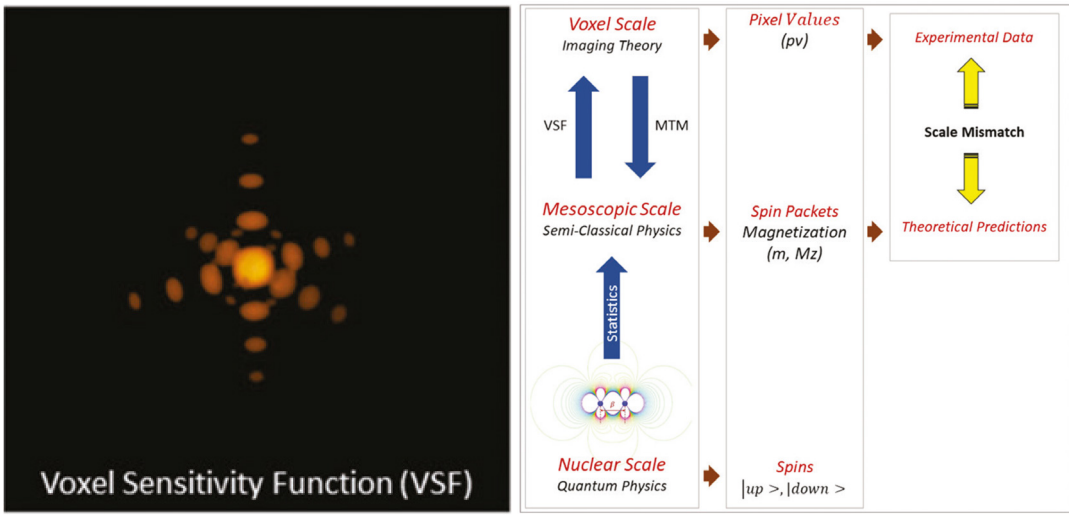

Figure 1: Spatial scales in MRI theory. (A) Three-dimensional rendering of the theoretical voxel shape in Fourier MRI as represented by the voxel sensitivity function. (B) Three spatial scales and the associated theories: from quantum physics of dipolar interactions between individual spins (bottom) to semiclassical physics describing spin packets with use of the Bloch equation (middle) to imaging theory describing voxels (top). Microstructural tissue modeling (MTM) is a venue for deconstructing voxels into spin packets. Knowing the voxel sensitivity function can be useful for modeling the actual intravoxel structure and providing a link between the mesoscopic and voxel scales.

cerebrospinal fluid (CSF); however, its accuracy diminishes with increasing tissue complexity. Furthermore, the BPP theory did not account for the T_1 contribution to T_2. Consequently, the BPP theory leads to T_2 overestimation for CSF well over experimental values of T_2 = 2.9 seconds at 37°C (36–38). The theoretical extension by Dixon et al (40) included this T_2 relaxation mechanism, resulting in the spin-packet (ie, sp) formula:

$$\left(\frac{1}{T_2}\right)_{sp} = \left(\frac{1}{T_2^{BPP}}\right)_{sp} + \frac{1}{2}\left(\frac{1}{T_1^{BPP}}\right)_{sp} \quad (1).$$

As shown by computer simulations (Fig 2), Equation (1) combined with the BPP relaxation rate equations (41) correctly predict $(T_2)_{sp}<(T_1)_{sp}$ for CSF at τ_c of 1.5 psec. The first term in Equation (1) is the adiabatic term and represents the relaxation rate due to loss of signal coherence caused by dephasing processes, and the second nonadiabatic term is the T_1 contribution to T_2 that results from the loss of signal-generating spins in the transverse state, which occurs at a rate of $(R_1)_{sp}/2$.

Fast-Exchange Two-State Tissue Model

The nonaqueous tissue components of the central nervous system (ie, lipids, proteins, and nucleic acids) account for 15%–30% of its mass (42). The other 70%–85% is of four types: CSF spaces, intracellular water, extracellular water, and water between myelin bilayers. The MR properties of these water pools are different and present increasing theoretical modeling complexities, from CSF to intra- or extracellular water to water between myelin bilayers.
The BPP-Dixon theory accurately predicts the T_1 and T_2 values of healthy CSF. However, relaxation phenomena are complicated for gray matter (GM) and more so for white matter (WM) due to the intricate relaxation-MT effects of myelin. GM-WM contrast in most MRI sequences is known to reflect mainly the spatial distributions of myelin and iron, which have been shown to overlap in many brain regions, particularly in the cortex (43). The B_0 dependencies of $1/T_1$ and $1/T_2$ of unmyelinated brain tissue can be explained with the fast-exchange twostate model (41), which assumes two spin-packet types: a waterlike free pool with a B_0-independent T_{1f} value close to tap water (approximately 2–3

seconds) (41) and a much smaller bound pool fraction with B0-dependent T_{1b}. The two pools exchange water molecules with a short residence time in the bound state on the nanosecond scale. In the fast-exchange two-state model, $1/T_1$ is determined predominantly by molecular interactions between macromolecules and a bound hydration layer, and $1/T_2$ is governed mainly by the exchange diffusion of water between the bound layer and a free water phase. Despite the high tissue complexity, relatively straightforward empirical formulas can be used for describing the main dependencies of $1/T_1$ and $1/T_2$ on B_0, myelin, and iron content (41,44–47).

Multi–Proton Pool Models

Myelinated tissue modeling at the nanometer scale would be a formidable undertaking even if the underlying microanatomic blueprints were accessible in vivo with use of hypothetical ultra–high spatial resolution MRI. This is currently the realm of ex vivo technologies, such as electron beam microscopy (Fig 3), which necessitates ex vivo samples placed in a vacuum.

A practical tissue modeling strategy is to forgo the intravoxel positional information of individual spin packets and instead categorize these by T_2; this leads to the concept of proton pools of "equivalent" spin packets.

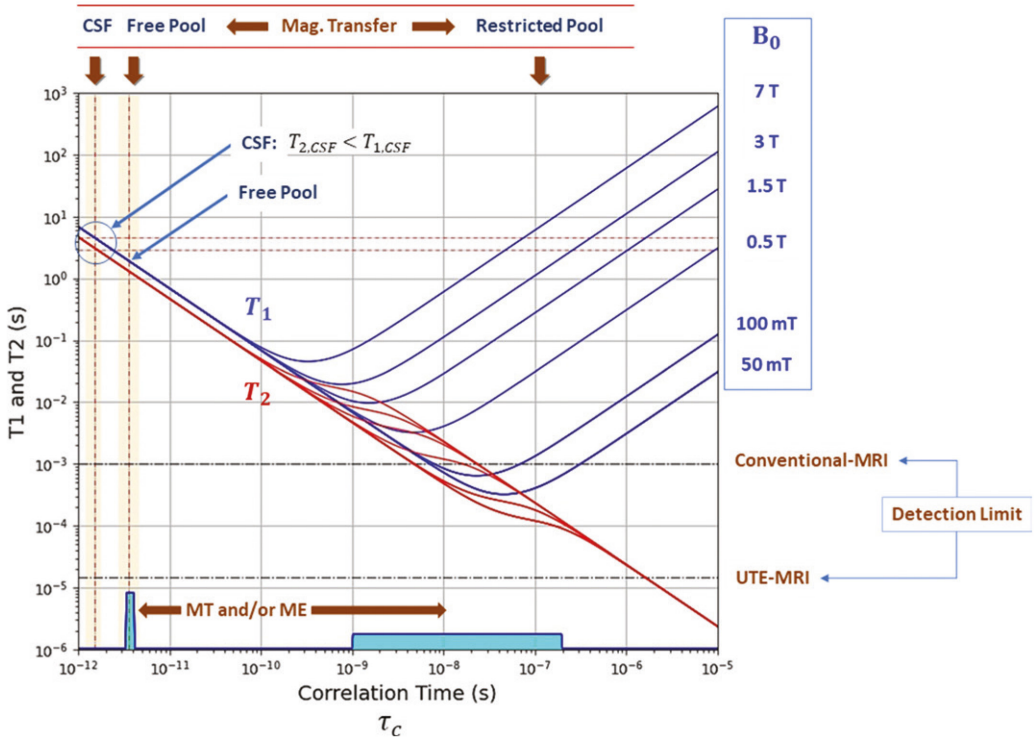

Figure 2: Bloembergen, Purcell, and Pound–Dixon theory. Computer simulations show T_1 and T_2 curves as functions of the correlation time (τ_c) for several values of the main magnetic field in the range of 50 mT to 7.0 T. In the short correlation time regimen of cerebrospinal fluid (CSF) and the free pool of tissue, the T_1 and T_2 curves are independent of B0 and decrease as functions of increasing correlation time. Following a transition range, the T_1 and T_2 curves show opposite dependencies on the correlation time. These curves are valid for ^{1}H nucleus in any tissue environment at the spatial scale of spin packets, but not necessarily at the much larger spatial scale of voxels, depending on the spatial scalability of the voxel. A typical tissue would have a distribution of correlation times such as the one shown in cyan: free (narrow peak) and potentially broad macromolecular feature. Interpool magnetization transfer (MT) and/or magnetization exchange (ME) effects lead to B0 dependencies of the relaxation times. Horizontal lines indicate the detection limits for conventional MRI (T_2,>1 msec) and ultrashort echo time (UTE-MRI) (T_2,>15 μsec). Mag = magnetic.

to the concept of proton pools of "equivalent" spin packets. Mapping the properties of these pools can provide important indicators of tissue microstructure. The motion-restricted pool of protons within larger molecules, such as non queous myelin protons, is not directly detectable because of their short T_2s but has a major influence on tissue relaxation and signal through rapid MT and/or magnetization exchange processes with freer pools (Fig 4). To illustrate the current state-of-the-art refinement in multipool WM modeling using ex vivo experimentation, consider the four-pool model studied by Manning et al (47). The model (Fig 3) includes protons of nonaqueous myelin (pool 1), water between myelin bilayers (pool 2), intra- and extracellular water (pool 3), and nonaqueous nonmyelin protons (pool 4). In vivo imaging of multipool relaxation phenomena at such a level of complexity is not practical with current clinical technologies.

The simpler binary spin-bath model (48–51) has been widely applied to MT acquisitions, where off-resonance saturation is used to saturate the restricted large molecule pools. It describes voxels containing two proton pool types: free with a narrow bandwidth and bound with a broad bandwidth (Fig 4). In this case, the number of qMRI parameters to be determined is more manageable: *(a)* measures of PD of the free and the motion-restricted proton pools and *(b)* measures of magnetic interactions between protons and the molecular environment as well as magnetic interactions between the free and restricted pools.

Substantial progress has been made in this field in the past 20 years. Paraphrasing a recent review article by Sled (51), MT contrast is well established among the tools for assessing tissue microstructure in the brain. While much of the work has made use of MT ratios, improvements in the technology for rapidly acquiring MT-weighted images have made

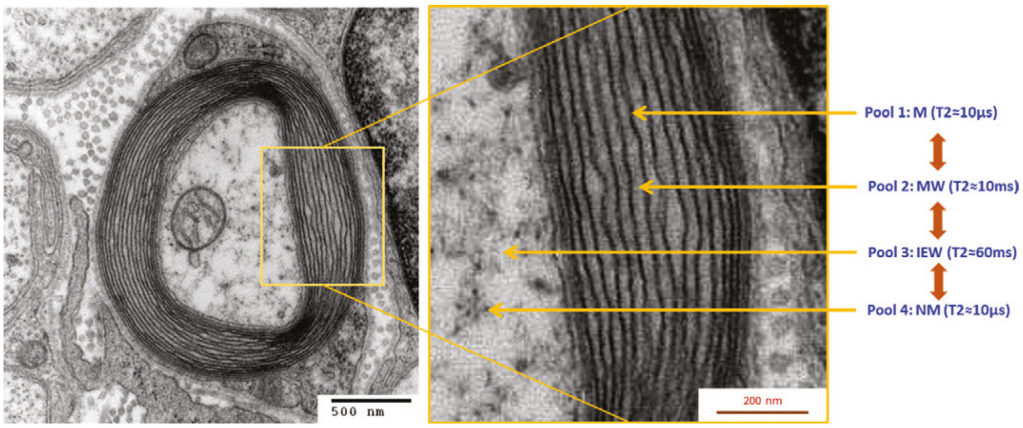

Figure 3: The four-pool model of white matter. The four ^{1}H-nuclei pools are depicted with use of a transmission electron micrograph of a myelinated axon in cross-section. The myelin layer (concentric) surrounds the axon of a neuron, showing cytoplasmatic organs inside. The nonaqueous pools 1 and 4 are detectable only with ultrashort echo time pulse sequences due to the extremely short T_2s. The micrograph of this cadaveric tissue sample was generated and deposited into the public domain by the Electron Microscopy Facility at Trinity College, Hartford, Connecticut (http://www.trincoll.edu). IEW = intra- and extracellular water, M = myelin protons, MW = myelin water, NM = nonmyelin protons.

the quantification of MT model parameters feasible within a clinically compatible scan time. Further characterization of the restricted large molecular pool is also proving possible. Introduced in the past decade, inhomogeneous MT contrast (52) reflects the presence and decay of a property known as dipolar order (53), which can provide new information on the structure and mobility of the restricted pool. It has the potential to expand these applications by improving the specificity, for example, to assess cortical myeloarchitecture (54). Methods for including quantitative introduced inhomogeneous MT into MRF studies have also been introduced (55).

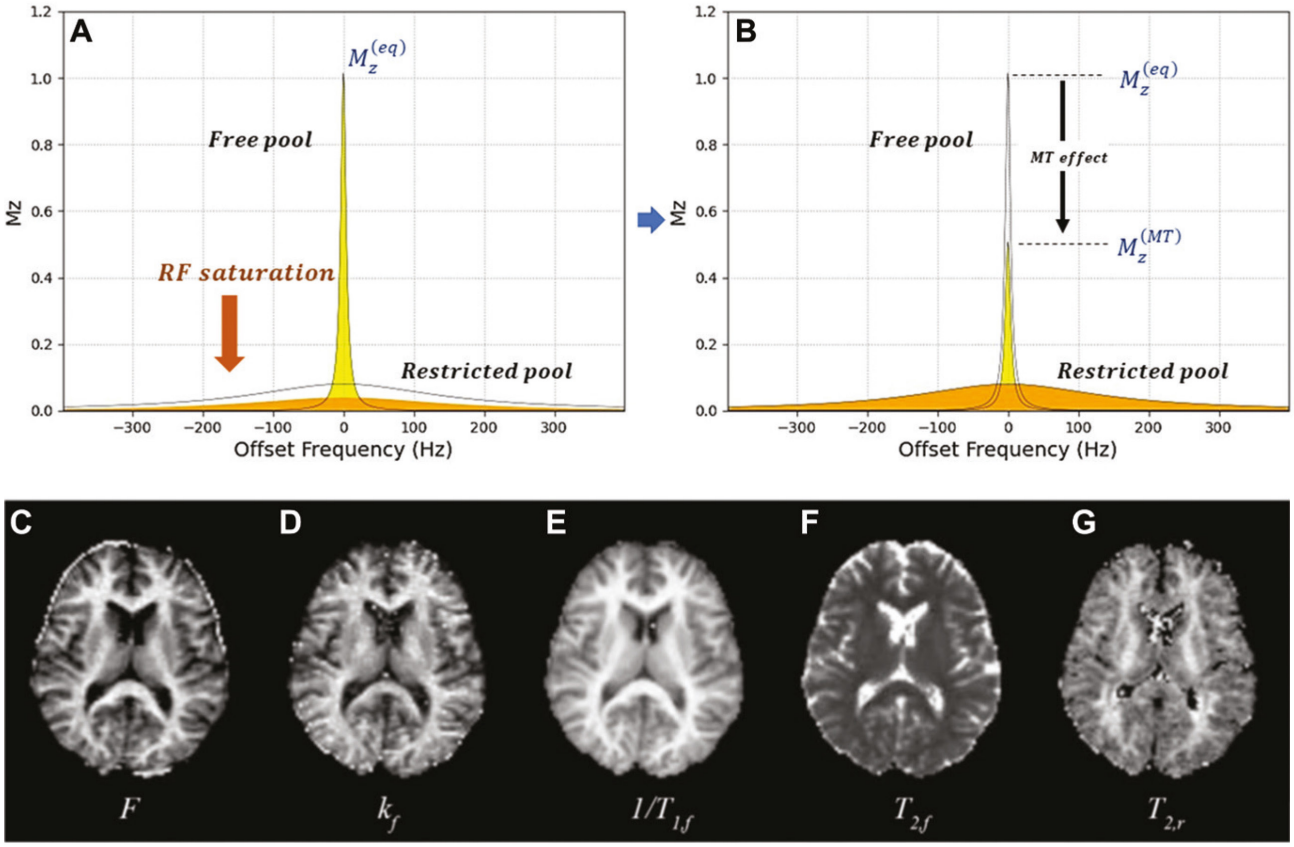

Figure 4: Magnetization transfer (MT) basics. (A, B) Graphs of the free and the restricted-motion pools illustrate the simplest MT imaging experiment in which an off-resonance radiofrequency pulse (red arrow) is used to saturate the semisolid pool (A), resulting subsequently in a net decrease of the liquid pool proton density (B) available for signal generation, hence additional MT contrast. M_z = z-component of the magnetization. (C–G) Quantitative MT images of the adult human brain in the axial plane. The parameter maps shown are the pool size ratio F, forward exchange rate kf, spin-lattice relaxation rate of the free pool, spin-spin relaxation rate of the free pool, and spin-spin relaxation rate of the restricted-motion pool. (Brain images reproduced from reference 51. Note: The referenced article is available under the Creative Commons CC-BY-NC-ND license, which permits noncommercial use of the work as published, without adaptation or alteration, provided the work is fully attributed.)

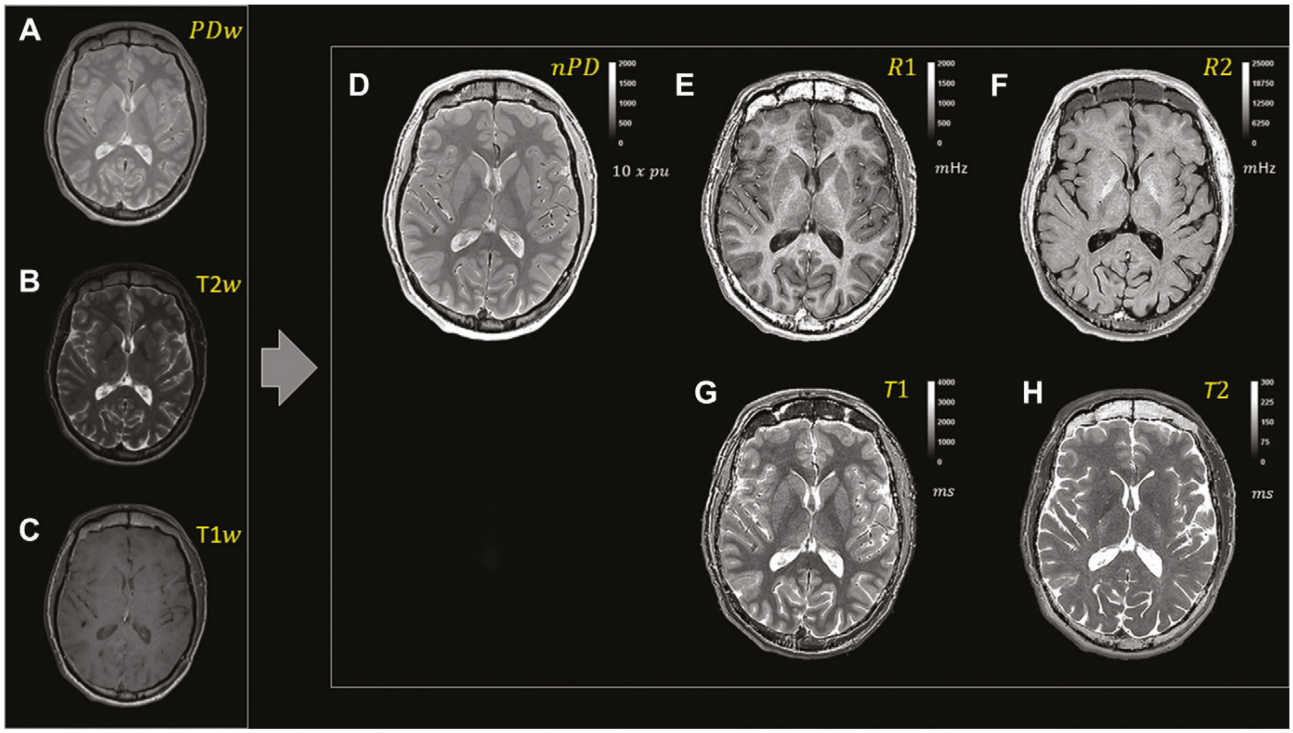

Figure 5: Multiparametric quantitative MRI (MP-qMRI) example with the triple turbo spin-echo pulse sequence. Same-section directly acquired images and quantitative+MRI parameter maps in the axial plane. The left column shows the three images directly acquired with (A) proton density weighting (PDw), (B) T_2 weighting (T_2w), and+(C) T_1 weighting (T_1w). The insert on the right shows the same-section MP-qMRI maps: (D) the cerebrospinal fluid–normalized proton density map (nPD) and (E, F)relaxation rate maps. Note that the inverse white matter (WM)–to–gray matter contrast in the relaxation rate maps versus (G, H) the relaxation time maps, in which WMis not only brighter but also shows marked texture. Furthermore, the WM texture of the longitudinal relaxation rate (R_1) map is different from that in the transverse relaxationrate (R_2) map. All images are in a 35-year-old healthy male volunteer and were acquired with the 9-minute scan (80 contiguous sections; reconstructed voxel = 0.5 x 0.5 x 2 mm) used for the ELGAN-ECHO (Extremely Low Gestational Age Newborns–Environmental influences on Child Health Outcomes) study (103).

MP-qMRI Frameworks

Rapid MP-qMRI

The workflow of MP-qMRI frameworks generating separate volumes representative of Np parameters with matrix size = (N_x, N_y, N_z) is:

$$\text{Patient} \xrightarrow{\text{Acquisition}} N_{\text{acq}} \xrightarrow{\text{Image Processing}} N_{\text{total}} = N_p\, N_x\, N_y\, N_z \quad (2).$$

The initial experimental data consist of N_{acq} signal samples in the Fourier domain, and the MP-qMRI processing workflow can include regridding for noncartesian acquisitions, inverse Fourier transformation, and parameter estimation. Conventional MP-qMRI frameworks (Table 1) first generate full-frame weighted images that can be interpreted clinically, and in a second step, these images are processed for parameter map generation. In contradistinction, direct frameworks (Table 2) do not generate the intermediate full-frame images and proceed to parameter mapping directly. Methods for shortening the time of acquisition of MPqMRI pulse sequences are key for promoting clinical acceptance. Also crucial is the development of accurate and automated image processing methods with short processing times. Reducing N_{acq} and/or reducing the effective time between samples (Δt_{eff}) results in a shorter time of acquisition $(\text{TA} = N_{\text{acq}}\, \Delta t_{\text{eff}})$.

The most measurement-efficient pulse sequences have echoplanar imaging readouts or hybrid spin-echo readouts, including rapid acquisition with relaxation enhancement, fast (or turbo) spin-echo, or fast gradient-echo sequences, which can also operate in the steady state. Additionally, simultaneous multislice techniques can be used to further accelerate two-dimensional pulse sequences (56,57). Techniques for reducing N_{acq} include parallel imaging using receiver coil spatial encoding (58) and compressed sensing using sparse acquisitions (59). Not surprisingly, rapid MP-qMRI frameworks (Tables 1, 2) use combinations of the aforementioned fast techniques.

Fast Indirect (Conventional) Frameworks

Neglecting partial volume effects, radiofrequency transmit inhomogeneities, and off-resonance effects, the weighted pixel values (ie, pv) are modeled as:

$$\text{pv}_{\text{voxel}} = \text{PD}_{\text{voxel}}\, \text{psw}(\text{TR}, \text{TE}, \text{FA}, \ldots | \text{T1}_{\text{voxel}}, \text{T2}_{\text{voxel}}, \ldots)\, \text{RP}_{\text{voxel}}\, \delta V + \text{Noise}_{\text{voxel}} \quad (3),$$

where PD_{voxel} is the main anatomic factor and is multiplied by two spatially dependent factors. First, the pulse sequence weighting factor (ie, psw) is a function of scanner control variables and the qMRI parameters. Scanner control variables include the repetition time (TR), the echo time (TE), and the flip angle (FA). Second, the receiver coil sensitivity profile, RP_{voxel}, is a smoothly varying function of space and represents an important source of uncertainty in PD mapping. The voxel volume is denoted by δV.

Other than PD, most qMRI tissue parameters can be quantified by differential weighting, which is a general qMRI principle motivated by Equation (3). Two or more images differing only in their weighting to the targeted parameter are acquired with otherwise identical experimental settings and processed with an algorithm that estimates the qMRI parameter value (Fig 5) that accounts for the weighting differences between the input images (Table 1). qMRI by

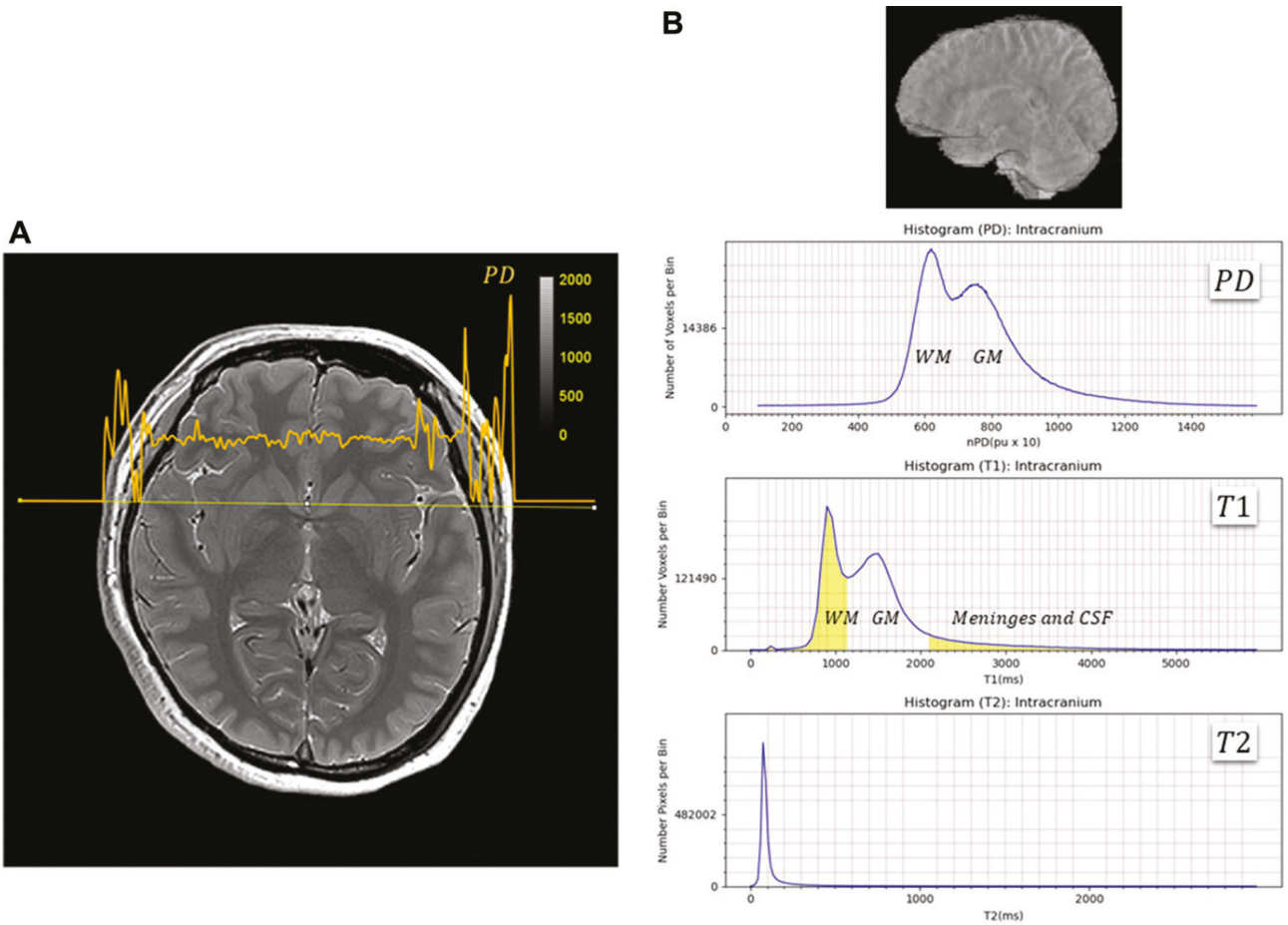

Figure 6: Proton density (PD) mapping. (A) PD map generated with the triple turbo spin-echo pulse sequence and the processing steps outlined in the text. Note that the superimposed single-line profile shows negligible residual coil profile effects. (B) Whole-brain histograms of PD, T_1, and T_2 for generated with triple turbo spin-echo (80 consecutive sections; voxel = 0.5 x 0.5 x 2 mm; scan time, approximately 9 minutes). Accuracy of the PD map is further ascertained by the very similar bimodal PD histogram shape compared with the T_1 relaxogram below, which is consistent with the empirical 1/PD $\propto$ 1/T_1 relationship that holds for healthy brain tissue (see text). This map is in a 41-year-old healthy female volunteer and was acquired with the same protocol used for the ELGAN-ECHO (Extremely Low Gestational Age Newborns–Environmental influences on Child Health Outcomes) study (103). CSF = cerebrospinal fluid, GM = gray matter, WM = white matter.

differential weighting is useful because it effectively removes extraneous information from the parameter estimates, and, most importantly, it removes inaccuracies caused by inhomogeneities in receiver coil sensitivity profile.

The accuracy of PD mapping is paramount, as it reports on water content and provides the anatomic substrate for synthetic MRI. PD mapping proceeds in three steps: (*a*) reversing the weightings to T_1 and T_2 (or T_2^*) of a directly acquired image selected based on the highest signal-to-noise ratio and overall image quality, (b) correcting the coil receiver profile (60), and (*c*) scaling the PD map to a spatially invariant factor that calibrates all pixel values relative to a known pixel value, usually an external sample within the field of view or that of healthy CSF. PD mapping difficulties stem primarily from residual uncertainties in the T_1 and T_2 (or T_2^*) estimates, imperfections of the pulse sequence model (particularly in the estimation of actual flip angles and insufficiently spoiled CSF signals), and unaccounted intrinsic MT effects. In the healthy brain, 1/PD is proportional to 1/T_1 (61–65), and this simple relationship provides an additional method for checking PD mapping accuracy (Fig 6). Detection sensitivity of short T_2 species can be by indirect means via MT imaging (47) or directly with ultrashort echo time pulse sequences (ie, echo time > 15 μsec). PD measures obtained with standard pulse sequences defined as echo time less than 1 msec are underestimations of the total PD, which additionally includes slowly moving aqueous protons as well as nonaqueous protons (up to 30% in WM). Nonaqueous species, including protons of lipids, proteins, and nucleic acids, become visible in the ultrashort echo time regimen (66). Ample experimental evidence on deviations from simple exponential relaxation has led to techniques for quantifying myelin water content (29,42,67), a biologic marker for conditions affecting myelin.

Fast indirect MP-qMRI frameworks use regular weighted pulse sequences modified to acquire several weighted images per scan. Such directly acquired images have different weightings on the target qMRI parameters and bear identical geometry and receiver gain settings. Multiple frameworks using variations of clinical pulse sequences, from rapid gradient-echo to steady-state to rapid acquisition with relaxation enhancement (fast [turbo] spin-echo) pulse sequences, are listed in Tables 1 and 2.

Voxel Types and Partial Volume

Three voxel types posing distinct qMRI processing complexities are conceptualized (Fig 7). Type 1 voxels of pure CSF are fully scalable from spin packet to voxel and are devoid of MT effects; however, qMRI processing difficulties arise because of the exceptionally long T_1 of 4.5 seconds and T_2 of 2.9 seconds for CSF. Most fast qMRI pulse sequences (Table 1) generate strong differential

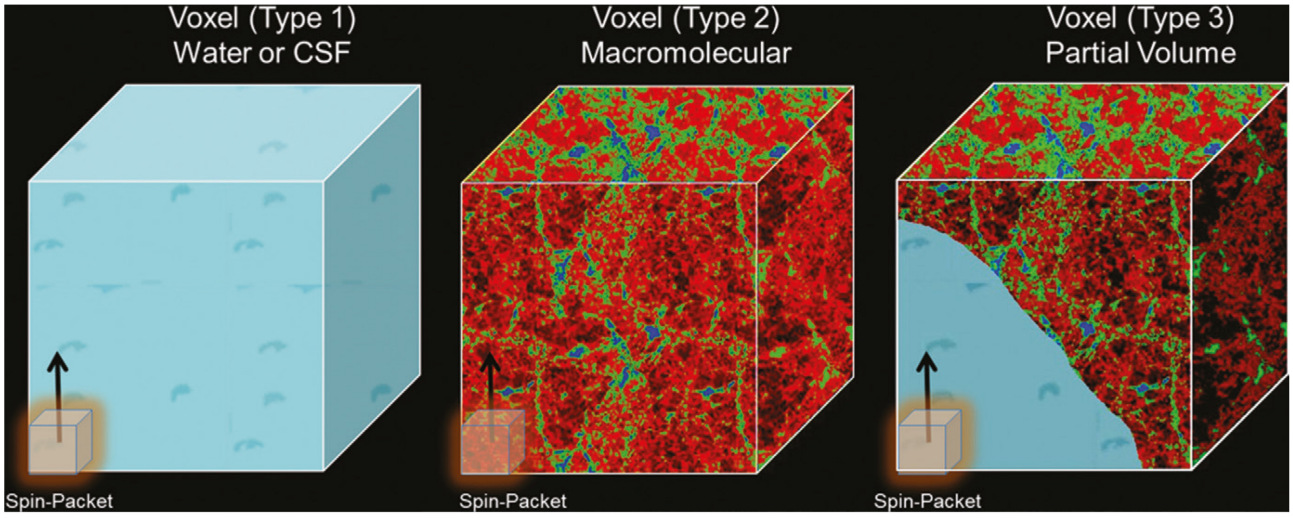

Figure 7: Voxel types according to spatial scalability. Three different voxel types with increasing inner complexity from left to right (simulation colors: blue = cerebrospinal fluid [CSF], red = gray matter [GM], green = white matter [WM]). Type 1, which contains pure CSF (left), is fully scalable, meaning that the quantitative MRI (qMRI) parameters at the spin-packet and voxel scales are equal. Type 2 voxels contain a typical structured soft tissue (eg, WM or GM), leading to a distribution of correlation times and magnetization transfer effects, as reviewed in the text. Type 3 voxels are difficult for qMRI algorithms because of partial volume effects.

weighting between WM and GM but not necessarily for CSF, which has extremely long T_1 and T_2 relaxation times. Such limitations need to be addressed, since healthy CSF can serve as a qMRI reference irrespective of pulse sequence – without MT effects – and field strength.

Type 2 macromolecular voxels containing WM and GM account for the great majority of voxels in the brain. qMRI processing difficulties stem primarily from the intricate intravoxel architecture, thus necessitating multipool models and MT considerations. Furthermore, given the fact that BPP spin-packet formulas cannot be scaled up to voxels without knowledge of the intravoxel microarchitecture, additional mathematical developments along the lines described in diffusion research (25) are needed.

Type 3 voxels are CSF–brain tissue partial-volume voxels that present a challenge for qMRI algorithms, often resulting in inaccuracies and artifacts in the form of bright outlier pixels near boundaries (Fig 8), which contribute to deterring routine clinical use of qMRI maps for diagnosis.

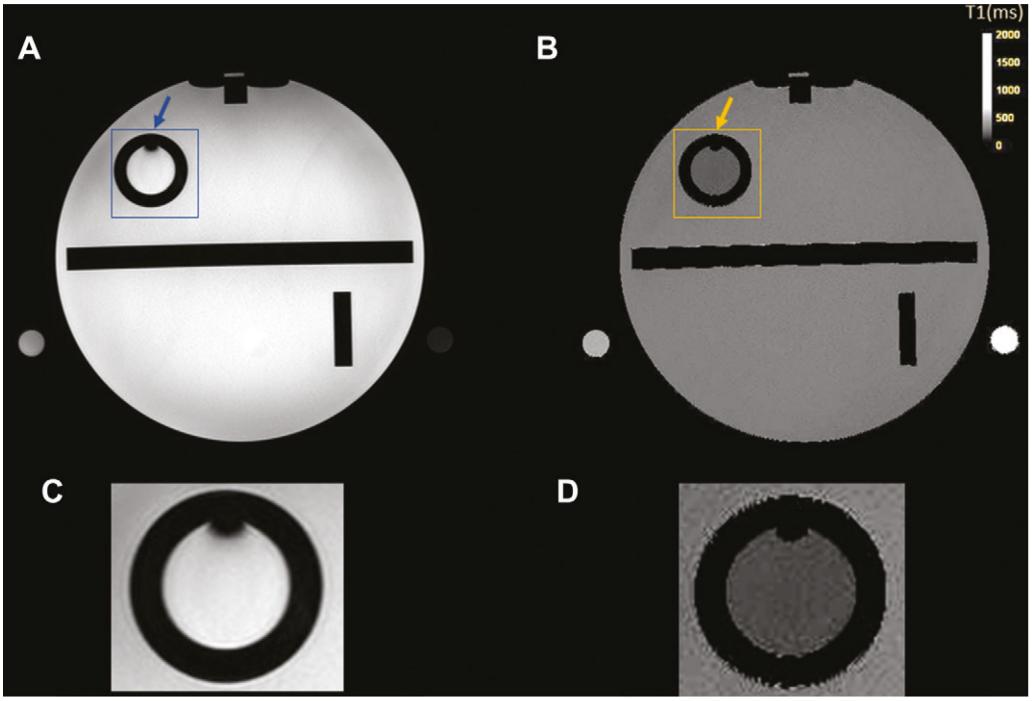

Figure 8: Partial volume artifacts. (A) T_1-weighted image is compared with (B) the corresponding T_1 map of the American College of Radiology MRI accreditation phantom. The arrows and outlines in A and B correspond to the magnifications in (C) and (D), respectively. Even though the T_1 map has less intensity variation, bright pixels near the edges (see magnifications) result in a less natural appearance. As discussed in the text, improving the visual appearance of quantitative MRI (qMRI) maps is very important for the clinical adoption of qMRI.

Fast Direct Frameworks

MR Fingerprinting

In MRF, multiple pulse sequence control variables are varied pseudorandomly throughout the acquisition to sensitize the signal to the targeted qMRI parameters. The resulting experimental fingerprints have distinctive sensitization patterns to the targeted parameters. In a typical implementation, the qMRI algorithm takes the experimental fingerprints and finds the closest theoretical fingerprints within a prebuilt dictionary of simulated signal evolutions associated with a particular combination of qMRI parameters. Accordingly, pattern recognition algorithms are used to select appropriate tissue properties for each voxel (68). The balanced steady-state free precession pulse

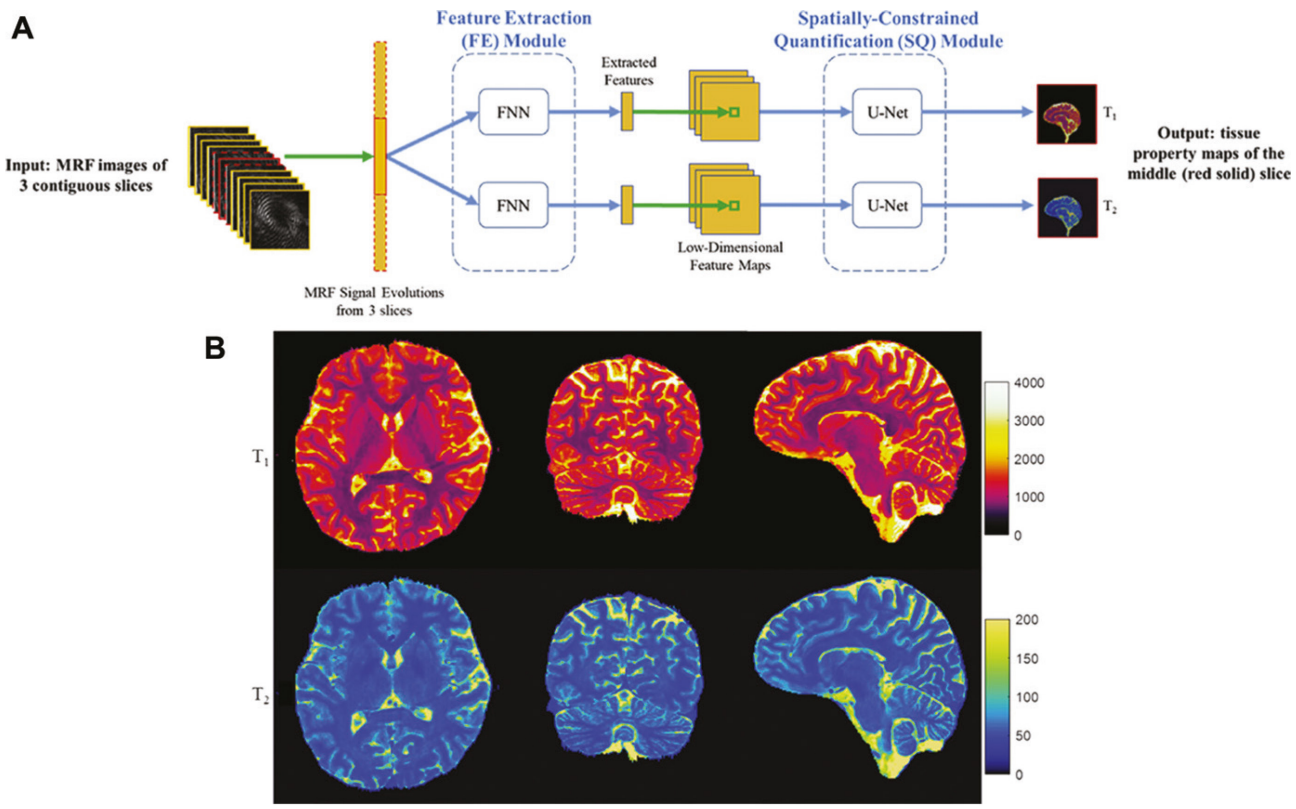

Figure 9: Schematic overview of the convolutional neural networks model with two modules for tissue property mapping. (A) The feature extraction module consists of four fully connected layers (FNNs), which is designed to mimic singular value decomposition to reduce the dimension of signal evolutions. The U-Net structure was used for the spatially constrained quantification module to capture spatial information from neighboring pixels for improved quantification of tissue properties. MR fingerprinting (MRF) images of three contiguous sections (red) were used as input, and the corresponding reference T_1 and T_2 maps from the central section were used as output for the network. (B) Reformatted quantitative maps in axial, coronal, and sagittal views from the prospectively accelerated scan (three-dimensional MRF, standard; R = 2; 192 time points). The acquisition time for 176 sections was about 7 minutes. (From reference 20. Note: The referenced article is available under the Creative Commons CC-BY-NCND license, which permits noncommercial use of the work as published, without adaptation or alteration, provided the work is fully attributed.)

sequence was used in the original and seminal MRF publication (21). Further research proceeded to replace MRF–balanced steady-state free precession with the steady-state free precession sequence, which acquires coherent steady-state signals with a constant unbalanced gradient moment in each repetition time, thus reducing banding artifacts. The steady-state free precession sequence does not lead to such banding artifacts (22). Further research by Chen et al
(20) with the integration of parallel imaging and deep learning techniques led to a rapid three-dimensional MRF method with a spatial resolution of 1 mm3, which could provide whole-brain T_1 and T_2 maps in approximately 7 minutes (Fig 9).

Multitasking MP-qMRI

A recently developed MP-qMRI framework achieves three-dimensional combined brain T_1, T_2, and apparent diffusion coefficient (ADC) mapping by incorporating diffusion preparation and phase correction into the T_1 and T_2 MR multitasking framework (7,8). The three weightings are generated by means of pulse sequence preparation modules. Reported advantages include the mitigation of physiologic motion sensitivity relative to the double echo with steady state because only the preparation modules are sensitive to physiologic motion, as opposed to each signal readout. Furthermore, compared with MRF and stimulated echo–based mapping (69), the multitasking framework achieves comprehensive T_1, T_2, and ADC quantification (Fig 10) with three noncolinear diffusion directions, thus matching the standard clinical diffusion-weighted imaging protocol. In its current implementation, it achieves 100-mm coverage (20 sections) in 9.3 minutes.

MP-qMRI Applications

The scope of MP-qMRI applications for neuroimaging may not be fully predicted at this early stage of development. At the current rapid pace of progress, the creation of a comprehensive MP-qMRI virtual central nervous system analog at high spatial resolution (approximately 0.25 mm^3) seems achievable in the not-so-distant future. With rapidly improving image processing techniques and continuous advances in computer hardware, MP-qMRI has the potential for improving MRI in ways that may not be fully envisioned at this time. Currently, three MP-qMRI applications emerge as logical contenders: synthetic MRI, macrostructural qMRI, and MTM.

Synthetic MRI

Synthetic MRI uses computer models of MRI pulse sequences to “scan” the virtual patient, thus generating images with arbitrary contrast weightings. Synthetic MRI was invented in the early 1980s (70,71). With the advent of faster MP-qMRI frameworks, interest in synthetic MRI is regaining momentum, in part to simplify and standardize clinical protocols and additionally to enable visual exploration of contrast weightings that may be more revealing of intravoxel tissue architecture and subtle pathologic abnormalities.

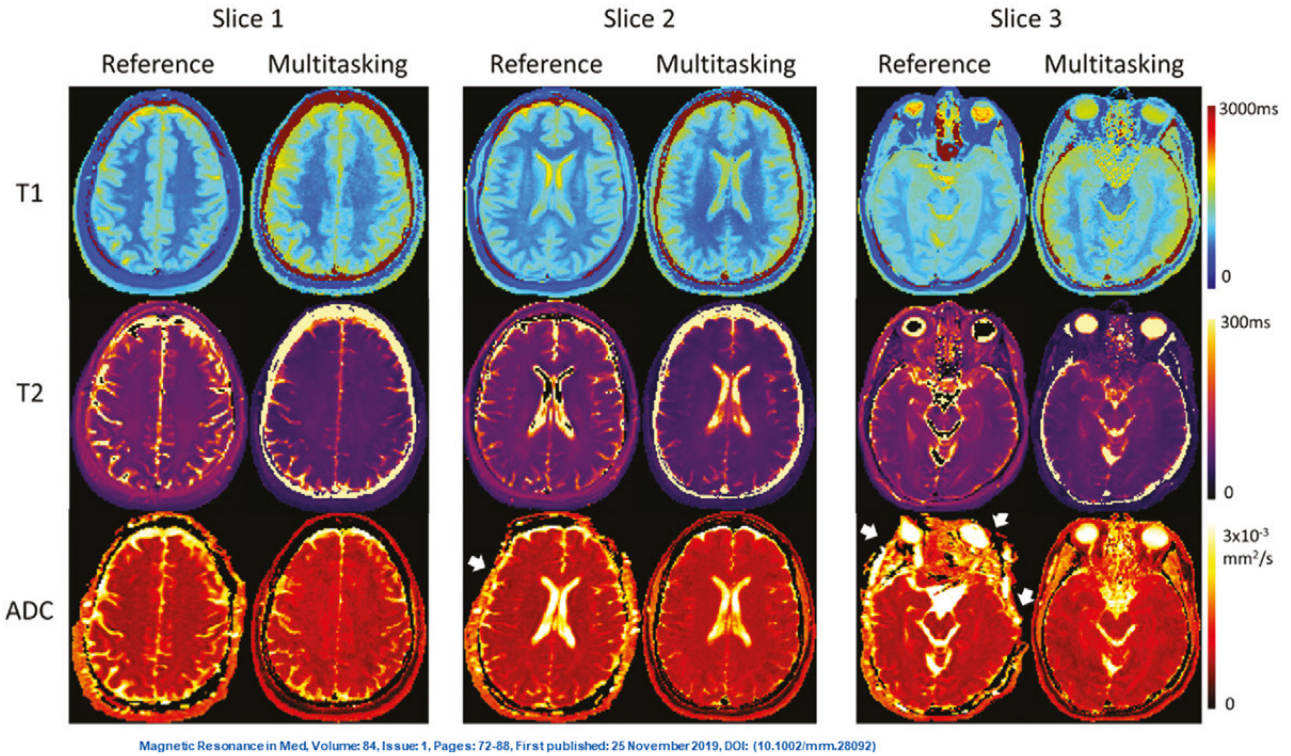

Figure 10: Representative in vivo T_1, T_2, and apparent diffusion coefficient (ADC) mapping of three sections with use of multitasking and the respective reference protocols in a healthy volunteer. Multitasking provides T_1, T_2, and ADC maps with good qualitative agreement with the references and without image distortion (white arrows), which can be observed on single-shot echoplanar imaging ADC maps. (Reprinted, with permission, from reference 7.)

Remarkably, some synthetic pulse sequences may not have a known clinical analog, such as pulse sequences weighted by the inverse of T_1, namely R_1. This can be used to bring out the underlying structural framework of WM (Fig 11) owing to its high average R_1 values of myelinated tissue.

Macrostructural qMRI

Macrostructural qMRI seeks to automatically detect and group voxels using simultaneously positional (x, y, z) and qMRI (eg, PD, T_1, T_2) attributes to classify them into segments associated with tissue types and/or organs. Such a rich set of voxel attributes can serve as classifiers for automated segmentation with use of multiclustering algorithms that are useful for parceling the brain into tissue segments (3). Tissue and/or organ volumetry and relaxographic qMRI with histograms can then be implemented automatically (Fig 6B), thus providing useful data constructs for comparing patients in multisite and longitudinal studies. The generated macromeasures can be useful for designing a standardized clinical qMRI report to support and complement the radiologic report, provided that normal qMRI parameter ranges have been established as functions of key modifiers such as age and sex.

Microstructural Tissue Modeling

MTM seeks to decode the intravoxel microarchitecture with use of computer modeling based on prior knowledge, as opposed to by increasing the spatial resolution of the scan, an approach that currently seems to be more limited in terms of resolution improvement potential. MTM offers the potential for assessing the intravoxel composition in terms of the building neuro-elements (somas, axons, myelin, dendrites, and glia); in other words, it has the potential for achieving noninvasive in vivo histologic examination (28).

MTM developments have been predominantly by means of dMRI (30) mainly applied to WM and, to a lesser extent, GM (72). Recent research studying the dependencies of T_1 microstructure is promising yet still not ready for in vivo applications (47).

Future Directions

Although most radiologists are aware of the potential benefits of using qMRI and that the technologies are approaching clinical and commercial deployment status, MP-qMRI of PD, T_1, and T_2 (T_2^*) has yet to achieve routine clinical use. We can learn from the implementation history of dMRI that the adoption of qMRI frameworks depends primarily on three factors, in order of importance: medical necessity with a critical clinical question, diagnostic efficacy and reproducibility, and technology availability.

In the case of dMRI, detection of early ischemia was the urgent clinical indication; ADC reduction was the indisputable and reproducible dMRI effect. Since then, dMRI has found numerous additional brain and body applications, particularly for tumor characterization (73).

Because examples of MP-qMRI frameworks have been described that incorporate ADC (Tables 1, 2), we may foresee that deploying four-dimensional MP-qMRI (PD, T_1, T_2, ADC) as spatially coregistered frameworks could provide a seamless clinical adoption avenue. Such efforts are further strengthened by organized efforts to develop rigorous scientific standards of PD, T_1, T_2, and ADC (74) as well as reliability and reproducibility (75) studies reporting encouraging results. Use of four-dimensional frameworks could come at no extra time-cost either at acquisition or image processing and would augment the diagnostic information for patients with stroke and cancer. It would further open quantification possibilities for clinical appli-

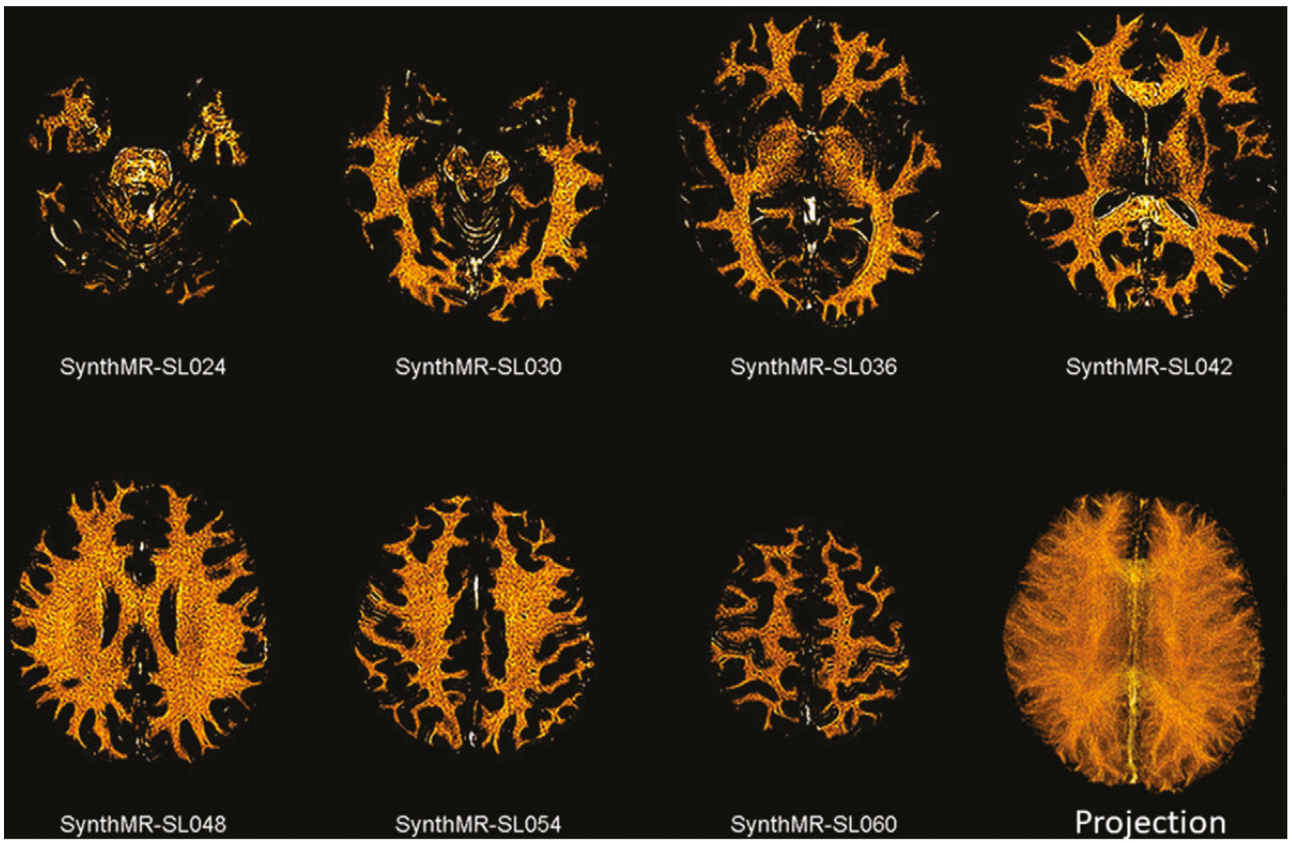

Figure 11: R_1 weighting. (A) Series of R_1-weighted synthetic MR (SynthMR) images exposing the underlying white matter (WM) texture. (B) Upon projection along the superior-to-inferior direction, a rendering resembling a WM fibrogram was generated. This association needs validation with ex vivo experiments. These synthetic images are in the same 41-year-old healthy female participant as in Figure 6. SL = section number.

cations uniquely suited to PD, T_1, and T_2 (T_2^*) qMRI, such as any application involving WM abnormalities (eg, myelin disorders), GM abnormalities (eg, iron accumulation), and abnormal watercontent (eg, edema). In addition, this would enable exploration of contrast weightings with synthetic MRI and pave the road for MTM applications that would provide microscopic insights on the tissue structure in neurologic disease.

Conclusion

Since the initial proposals of fast brain multiparametric quantitative MRI frameworks more than a decade ago, the field is at a transition point between research and development and clinical implementation, with some commercial implementations on the horizon. The building-block acquisition and processing technologies are well advanced to propel the field into a coherent clinical testing phase, with potential acceptance in the next decade if standardization agreements, quality control protocols, and theoretical clarifications occur.

Disclosures of conflicts of interest:
H.J. Grants from the National Institute of Neurological Disorders and Stroke, National Institutes of Health Office of the Director, and the National Institute of Child Health and Human Development; royalties from World Scientific; named inventor on patents for quantitative MRI and white matter fibrography owned by Trustees of Boston University and Boston Medical Center; member of the *Radiology* editorial board; uncompensated scientific advisor to Stratagen Bio. **O.S.** Consultancy with Boston Imaging Core Lab; payment for lectures from Bayer Yakuhin; royalties from Gakken Medical Shujunsha, Medical Sciences International. **E.F.** No relevant relationships. **A.M.O.P.** No relevant relationships. **N.J.S.** Royalties from the Royal Society of Chemistry. **D.C.A.** Research support from GE Healthcare; royalties through institution from GE Healthcare, Siemens Healthcare, Philips Healthcare, and United Imaging Healthcare America for patents related to arterial spin labeling MRI. **K.E.K.** No relevant relationships.

References

1. Seiler A, Nöth U, Hok P, et al. Multiparametric quantitative MRI in neurological diseases. Front Neurol 2021;12(287):640239.
2. Cho S, Jones D, Reddick WE, Ogg RJ, Steen RG. Establishing norms for age-related changes in proton T1 of human brain tissue in vivo. Magn Reson Imaging 1997;15(10):1133–1143.
3. Suzuki S, Sakai O, Jara H. Combined volumetric T_1, T_2 and secular-T_2 quantitative MRI of the brain: age-related global chan ges (preliminary results). Magn Reson Imaging 2006;24(7): 877–887.
4. Saito N, Sakai O, Ozonoff A, Jara H. Relaxo-volumetric multi-spectral quantitative magnetic resonance imaging of the brain over the human lifespan: global and regional aging patterns. Magn Reson Imaging 2009; 27(7): 895–906.
5. Yeatman JD, Wandell BA, Mezer AA. Lifespan maturation and degeneration of human brain white matter. Nat Commun 2014;5(1):4932.
6. Slator PJ, Palombo M, Miller KL, et al. Combined diffusion-relaxometry microstructure imaging: current status and future prospects. Magn Reson Med 2021;86(6): 2987–3011.
7. Ma S, Nguyen CT, Han F, et al. Three-dimensional simultaneous brain T_1, T_2, and ADC mapping with MR multitasking. Magn Reson Med 2020;84(1): 72–88.
8. Ma S. Simultaneous Quantitative Multiparametric MRI for in Vivo Tissue Characterization Using Magnetic Resonance Multitasking: Methodology and Clinical Experience. UCLA. https://escholarship.org/uc/item/0d5369hr. Published 2020. Accessed May 2022.
9. Le Bihan D, Johansen-Berg H. Diffusion MRI at 25: exploring brain tissue structure and function. Neuroimage 2012;61(2):324–341.
10. Sullivan DC, Obuchowski NA, Kessler LG, et al. Metrology standards for quantitative imaging biomarkers. Radiology 2015;277(3):813–825.
11. Bloch F. Nuclear induction. Phys Rev 1946;70(7-8):460–474.
12. McConnell H. Reaction rates by nuclear magnetic resonance. J Chem Phys 1958;28(3):430–431.
13. Torrey H. Bloch equations with diffusion terms. Phys Rev 1956; 104(3):563–565.
14. Graumann R, Fischer H, Oppelt A. A new pulse sequence for determining T_1 and T_2 simultaneously. Med Phys 1986;13(5):644–647.
15. In den Kleef JJ, Cuppen JJ. RLSQ: T_1, T_2, and rho calculations, combining ratios and least squares. Magn Reson Med 1987;5(6):513–524.
16. Just M, Thelen M. Tissue characterization with T_1, T_2, and proton density values: results in 160 patients with brain tumors. Radiology 1988;169(3):779–785.
17. Haase A. Snapshot FLASH MRI. Applications to T_1, T_2, and chemicalshift imaging. Magn Reson Med 1990;13(1):77–89.
18. Lee JN, Riederer SJ. The contrast-to-noise in relaxation time, synthetic, and weighted-sum MR images. Magn Reson Med 1987;5(1):13–22.
19. McPhee KC, Wilman AH. T_1 and T_2 quantification from standard turbo spin echo images. Magn Reson Med 2019;81(3):2052–2063.
20. Chen Y, Fang Z, Hung SC, Chang WT, Shen D, Lin W. High-resolution3D MR fingerprinting using parallel imaging and deep learning. Neuroimage 2020;206:116329.
21. Ma D, Gulani V, Seiberlich N, et al. Magnetic resonance fingerprinting. Nature 2013;495(7440):187–192.
22. Jiang Y, Ma D, Seiberlich N, Gulani V, Griswold MA. MR fingerprinting using fast imaging with steady state precession (FISP) with spiral readout. Magn Reson Med 2015;74(6):1621–1631.
23. Chen Y, Chen MH, Baluyot KR, et al. MR fingerprinting enables quantitative measures of brain tissue relaxation times and myelin water fraction in the first five years of life. Neuroimage 2019;186:782–793.
24. Gómez PA, Cencini M, Golbabaee M, et al. Rapid three-dimensional multiparametric MRI with quantitative transient-state imaging. Sci Rep 2020;10(1):13769.
25. Yablonskiy DA, Bretthorst GL, Ackerman JJH. Statistical model for diffusion attenuated MR signal. Magn Reson Med 2003;50(4):664–669.
26. Schyboll F, Jaekel U, Petruccione F, Neeb H. Dipolar induced spin-lattice relaxation in the myelin sheath: a molecular dynamics study. Sci Rep 2019;9(1):14813.
27. Jara H, Yu BC, Caruthers SD, Melhem ER, Yucel EK. Voxel sensitivity function description of flow-induced signal loss in MR imaging: implicationsn for black-blood MR angiography with turbo spin-echo sequences. nMagn Reson Med 1999;41(3):575–590.
28. Cercignani M, Bouyagoub S. Brain microstructure by multi-modal MRI: is the whole greater than the sum of its parts? Neuroimage 2018;182:117–127.
29. Does MD. Inferring brain tissue composition and microstructure via MR relaxometry. Neuroimage 2018;182:136–148.
30. Novikov DS, Fieremans E, Jespersen SN, Kiselev VG. Quantifying brain microstructure with diffusion MRI: theory and parameter estimation. NMR Biomed 2019;32(4):e3998.
31. Alexander DC, Dyrby TB, Nilsson M, Zhang H. Imaging brain microstructure with diffusion MRI: practicality and applications. NMR Biomed 2019;32(4):e3841.
32. Paus T. Imaging microstructure in the living human brain: a viewpoint. Neuroimage 2018;182:3–7.
33. Novikov DS, Kiselev VG, Jespersen SN. On modeling. Magn Reson Med 2018;79(6):3172–3193.
34. Dyrby TB, Innocenti GM, Bech M, Lundell H. Validation strategies for the ninterpretation of microstructure imaging using diffusion MRI. Neuroimage 2018;182:62–79.
35. Bloembergen N, Purcell E, Pound R. Relaxation effects in nuclear magnetic resonance absorption. Phys Rev 1948;73(7):679–712.
36. Hopkins AL, Yeung HN, Bratton CB. Multiple field strength in vivo T_1 and T_2 for cerebrospinal fluid protons. Magn Reson Med 1986;3(2):303–311.
37. Brooks RA, Di Chiro G. Magnetic resonance imaging of stationary blood: a review. Med Phys 1987;14(6):903–913.
38. Condon B, Patterson J, Jenkins A, et al. MR relaxation times of cerebrospinal fluid. J Comput Assist Tomogr 1987;11(2):203–207.
39. Gore JC, Anderson AW. The physics of relaxation. eMagRes 2013;2(1):67–78.
40. Dixon R, Ekstrand K, Moran P. Physical foundations of proton NMR: Part II—The microscopic description. In: Thomas SR, Dixon RL, eds. NMR in Medicine: The Instrumentation and Clinical Applications. American Association of Physicists in Medicine. Medical Physics Monograph No. 14. New York, NY: American Institute of Physics, 1986; 32. https://www.worldcat.org/title/nmr-in-medicine-the-instrumentationand-clinical-applications/oclc/14629645.
41. Bottomley PA, Foster TH, Argersinger RE, Pfeifer LM. A review of normal tissue hydrogen NMR relaxation times and relaxation mechanisms from 1-100 MHz: dependence on tissue type, NMR frequency, temperature, species, excision, and age. Med Phys 1984;11(4):425–448.
42. MacKay AL, Laule C. Magnetic resonance of myelin water: an in vivo marker for myelin. Brain Plast 2016;2(1):71–91.
43. Stüber C, Morawski M, Schäfer A, et al. Myelin and iron concentration in the human brain: a quantitative study of MRI contrast. Neuroimage 2014;93(Pt 1):95–106.
44. Cameron IL, Ord VA, Fullerton GD. Characterization of proton NMR relaxation times in normal and pathological tissues by correlation with other tissue parameters. Magn Reson Imaging 1984;2(2):97–106.
45. Fischer HW, Rinck PA, Van Haverbeke Y, Muller RN. Nuclear relaxation of human brain gray and white matter: analysis of field dependence and mimplications for MRI. Magn Reson Med 1990;16(2):317–334.
46. Rooney WD, Johnson G, Li X, et al. Magnetic field and tissue dependencies of human brain longitudinal $1H_2O$ relaxation in vivo. Magn Reson Med 2007;57(2):308–318.
47. Manning AP, MacKay AL, Michal CA. Understanding aqueous and nonaqueous proton T1 relaxation in brain. J Magn Reson 2021;323:106909.
48. Henkelman RM, Huang X, Xiang QS, Stanisz GJ, Swanson SD, Bronskill MJ. Quantitative interpretation of magnetization transfer. Magn Reson Med 1993;29(6):759–766.
49. Sled JG, Pike GB. Quantitative imaging of magnetization transfer exchange and relaxation properties in vivo using MRI. Magn Reson Med 2001;46(5):923–931.
50. Ramani A, Dalton C, Miller DH, Tofts PS, Barker GJ. Precise estimate of fundamental in-vivo MT parameters in human brain in clinically feasible times. Magn Reson Imaging 2002;20(10):721–731.
51. Sled JG. Modelling and interpretation of magnetization transfer imaging in the brain. Neuroimage 2018;182:128–135.
52. Varma G, Duhamel G, de Bazelaire C, Alsop DC. Magnetization transfer from inhomogeneously broadened lines: a potential marker for myelin. Magn Reson Med 2015;73(2):614–622.
53. Varma G, Girard OM, Prevost VH, Grant AK, Duhamel G, Alsop DC. Interpretation of magnetization transfer from inhomogeneously broadened lines (ihMT) in tissues as a dipolar order effect within motion restricted molecules. J Magn Reson 2015;260:67–76.

54. Munsch F, Varma G, Taso M, et al. Characterization of the cortical myeloarchitecture with inhomogeneous magnetization transfer imaging (ihMT). Neuroimage 2021;225:117442.
55. West DJ, Cruz G, Teixeira RPAG, et al. An MR fingerprinting approach for quantitative inhomogeneous magnetization transfer imaging. Magn Reson Med 2022;87(1):220–235.
56. Gagoski BA, Bilgic B, Eichner C, et al. RARE/turbo spin echo imaging with Simultaneous Multislice Wave-CAIPI. Magn Reson Med 2015;73(3):929–938.
57. Barth M, Breuer F, Koopmans PJ, Norris DG, Poser BA. Simultaneous multislice (SMS) imaging techniques. Magn Reson Med 2016;75(1):63–81.
58. Pruessmann KP, Weiger M, Scheidegger MB, Boesiger P. SENSE: sensitivity encoding for fast MRI. Magn Reson Med 1999;42(5):952–962.
59. Lustig M, Donoho D, Pauly JM. Sparse MRI: the application of compressed sensing for rapid MR imaging. Magn Reson Med 2007;58(6):1182–1195.
60. Mezer A, Rokem A, Berman S, Hastie T, Wandell BA. Evaluating quantitative proton-density-mapping methods. Hum Brain Mapp 2016;37(10):3623–3635.
61. Lorio S, Tierney TM, McDowell A, et al. Flexible proton density (PD) mapping using multi-contrast variable flip angle (VFA) data. Neuroimage 2019;186:464–475.
62. Meyers SM, Kolind SH, Laule C, MacKay AL. Measuring water content using T2 relaxation at 3T: phantom validations and simulations. Magn Reson Imaging 2016;34(3):246–251.
63. Abbas Z, Gras V, Möllenhoff K, Keil F, Oros-Peusquens AM, Shah NJ. Analysis of proton-density bias corrections based on T_1 measurement for robust quantification of water content in the brain at 3 Tesla. Magn Reson Med 2014;72(6):1735–1745.
64. Neeb H, Ermer V, Stocker T, Shah NJ. Fast quantitative mapping of absolute water content with full brain coverage. Neuroimage 2008;42(3):1094–1109.
65. Fatouros PP, Marmarou A. Use of magnetic resonance imaging for in vivo measurements of water content in human brain: method and normal values. J Neurosurg 1999;90(1):109–115.
66. Ma YJ, Jang H, Chang EY, et al. Ultrashort echo time (UTE) magnetic resonance imaging of myelin: technical developments and challenges. Quant Imaging Med Surg 2020;10(6):1186–1203.
67. Alonso-Ortiz E, Levesque IR, Pike GB. MRI-based myelin water imaging: a technical review. Magn Reson Med 2015;73(1):70–81.
68. Poorman ME, Martin MN, Ma D, et al. Magnetic resonance fingerprinting part 1: potential uses, current challenges, and recommendations. J Magn Reson Imaging 2020;51(3):675–692.
69. Zhang Y, Wells SA, Hernando D. Stimulated echo based mapping (STEM) of T_1, T_2, and apparent diffusion coefficient: validation and protocol optimization. Magn Reson Med 2019;81(1):167–181.
70. Ortendahl DA, Hylton NM, Kaufman L, Crooks LE. Signal to noise in derived NMR images. Magn Reson Med 1984;1(3):316–338.
71. Riederer SJ, Suddarth SA, Bobman SA, Lee JN, Wang HZ, MacFall JR. Automated MR image synthesis: feasibility studies. Radiology 1984;153(1):203–206.
72. Zhang H, Schneider T, Wheeler-Kingshott CA, Alexander DC. NODDI: practical in vivo neurite orientation dispersion and density imaging of the human brain. Neuroimage 2012;61(4):1000–1016.
73. Iima M, Le Bihan D. Clinical intravoxel incoherent motion and diffusion MR imaging: past, present, and future. Radiology 2016;278(1):13–32.
74. Keenan KE, Ainslie M, Barker AJ, et al. Quantitative magnetic resonance imaging phantoms: a review and the need for a system phantom. Magn Reson Med 2018;79(1):48–61.
75. Gracien RM, Maiworm M, Brüche N, et al. How stable is quantitative MRI? - Assessment of intra- and inter-scanner-model reproducibility using identical acquisition sequences and data analysis programs. Neuroimage 2020;207:116364.
76. Liu X, Feng Y, Lu ZR, Morrell G, Jeong EK. Rapid simultaneous acquisition of T_1 and T_2 mapping images using multishot double spin-echo EPI and automated variations of TR and TE (ms-DSE-PI-T12). NMR Biomed 2010;23(1):97–104.
77. Hutter J, Slator PJ, Christiaens D, et al. Integrated and efficient diffusionrelaxometry using ZEBRA. Sci Rep 2018;8(1):15138.
78. Manhard MK, Stockmann J, Liao C, et al. A multi-inversion multi-echo spin and gradient echo echo planar imaging sequence with low image distortion for rapid quantitative parameter mapping and synthetic image contrasts. Magn Reson Med 2021;86(2):866–880.
79. Oshio K, Jolesz FA. Simultaneous acquisition of proton density, T_1, and T_2 images with triple contrast RARE sequence. J Comput Assist Tomogr 1993;17(2):333–338.
80. Hua N, Horn M, Anderson S, Jara H. Tri-fast spin echo: a minimalistic crossplatform multi-spectral qMRI pulse sequence for routine clinical use [abstr]. In: Proceedings of the Twenty-Fifth Meeting of the International Society for Magnetic Resonance in Medicine. Berkeley, Calif: International Society for Magnetic Resonance in Medicine, 2017; 1499.
81. Warntjes JBM, Leinhard OD, West J, Lundberg P. Rapid magnetic resonance quantification on the brain: optimization for clinical usage. Magn Reson Med 2008;60(2):320–329.
82. Haacke EM, Chen Y, Utriainen D, et al. STrategically Acquired Gradient Echo (STAGE) imaging, part III: technical advances and clinical applications of a rapid multi-contrast multi-parametric brain imaging method. Magn Reson Imaging 2020;65:15–26.
83. Oros-Peusquens AM, Loução R, Abbas Z, Gras V, Zimmermann M, Shah NJ. A single-scan, rapid whole-brain protocol for quantitative water content mapping with neurobiological implications. Front Neurol 2019;10:1333.
84. Deoni SC, Rutt BK, Peters TM. Rapid combined T_1 and T_2 mapping using gradient recalled acquisition in the steady state. Magn Reson Med 2003;49(3):515–526.
85. Deoni SC, Peters TM, Rutt BK. High-resolution T_1 and T_2 mapping of the brain in a clinically acceptable time with DESPOT1 and DESPOT2. Magn Reson Med 2005;53(1):237–241.
86. Schmitt P, Griswold MA, Jakob PM, et al. Inversion recovery TrueFISP: quantification of T(1), T(2), and spin density. Magn Reson Med 2004;51(4):661–667.
87. Newbould RD, Skare ST, Alley MT, Gold GE, Bammer R. Three-dimensional T(1), T(2) and proton density mapping with inversion recovery balanced SSFP. Magn Reson Imaging 2010;28(9):1374–1382.
88. Ehses P, Seiberlich N, Ma D, et al. IR TrueFISP with a golden-ratio-based radial readout: fast quantification of T_1, T_2, and proton density. Magn Reson Med 2013;69(1):71–81.
89. Stöcker T, Keil F, Vahedipour K, Brenner D, Pracht E, Shah NJ. MR parameter quantification with magnetization-prepared double echo steadystate (MP-DESS). Magn Reson Med 2014;72(1):103-111.
90. Heule R, Ganter C, Bieri O. Triple echo steady-state (TESS) relaxometry. Magn Reson Med 2014;71(1):230–237.
91. Palma G, Tedeschi E, Borrelli P, et al. A novel multiparametric approach to 3D quantitative MRI of the brain. PLoS One 2015;10(8):e0134963.
92. Nguyen D, Bieri O. Motion-insensitive rapid configuration relaxometry. Magn Reson Med 2017;78(2):518–526.
93. Gras V, Farrher E, Grinberg F, Shah NJ. Diffusion-weighted DESS protocol optimization for simultaneous mapping of the mean diffusivity, proton density and relaxation times at 3 Tesla. Magn Reson Med 2017;78(1):130–141.
94. Heule R, Celicanin Z, Kozerke S, Bieri O. Simultaneous multislice tripleecho steady-state (SMS-TESS) T_1, T_2, PD, and off-resonance mapping in the human brain. Magn Reson Med 2018;80(3):1088–1100.
95. Shcherbakova Y, van den Berg CAT, Moonen CTW, Bartels LW. On the accuracy and precision of PLANET for multiparametric MRI using phase-cycled bSSFP imaging. Magn Reson Med 2019;81(3):1534–1552.
96. Shcherbakova Y, van den Berg CAT, Moonen CTW, Bartels LW. PLANET: an ellipse fitting approach for simultaneous T_1 and T_2 mapping using phase-cycled balanced steady-state free precession. Magn Reson Med 2018;79(2):711–722.
97. Cheng CC, Preiswerk F, Hoge WS, Kuo TH, Madore B. Multi-pathway multi-echo (MPME) imaging: all main MR parameters mapped based on a single 3D scan. Magn Reson Med 2019;81(3):1699–1713.
98. Lee H, Wehrli FW. Alternating unbalanced SSFP for 3D R.2 mapping of the human brain. Magn Reson Med 2021;85(5):2391–2402.
99. Mitchell DP, Hwang KP, Bankson JA, et al. An information theory model for optimizing quantitative magnetic resonance imaging acquisitions. Phys Med Biol 2020;65(22):225008.
100. Assländer J, Novikov DS, Lattanzi R, Sodickson DK, Cloos MA. Hybrid-state free precession in nuclear magnetic resonance. Commun Phys 2019;2(1):73.
101. Assländer J. A Perspective on MR fingerprinting. J Magn Reson Imaging 2021;53(3):676–685.
102. McNaughton RP, Pieper C, Sakai O, et al. Quantitative MRI characterization of the extremely preterm brain at adolescence: atypical versus neurotypical developmental pathways. Radiology 2022;304:419–428https:// doi.org/10.1148/radiol.210385.
103. ELGAN-ECHO study. https://elgan.fpg.unc.edu/elgan-echo-researchstudy. Accessed May 2022.